

Turbulent bifurcations in intermittent shear flows: From puffs to oblique stripes

Takahiro Ishida,¹ Yann Duguet,² and Takahiro Tsukahara¹

¹*Department of Mechanical Engineering, Tokyo University of Science, 278-8510 Chiba, Japan*

²*LIMSI-CNRS, Campus Universitaire d'Orsay, Université Paris-Saclay, 91405 Orsay, France*

(Received 8 February 2017; published 11 July 2017)

Localized turbulent structures such as puffs or oblique stripes are building blocks of the intermittency regimes in subcritical wall-bounded shear flows. These turbulent structures are investigated in incompressible pressure-driven annular pipe flow using direct numerical simulations in long domains. For low enough radius ratio η , these coherent structures have a dynamics comparable to that of puffs in cylindrical pipe flow. For η larger than 0.5, they take the shape of helical stripes inclined with respect to the axial direction. The transition from puffs to stripes is analyzed statistically by focusing on the axisymmetry properties of the associated large-scale flows. It is shown that the transition is gradual: as the azimuthal confinement relaxes, allowing for an azimuthal large-scale component, oblique stripes emerge as predicted in the planar limit. The generality of this transition mechanism is discussed in the context of subcritical shear flows.

DOI: [10.1103/PhysRevFluids.2.073902](https://doi.org/10.1103/PhysRevFluids.2.073902)

I. INTRODUCTION

Subcritical wall-bounded shear flows have the ability to sustain turbulent motion despite the linear stability of the laminar regime. As the flow rate is decreased starting from the fully turbulent regime, partial relaminarization is frequently observed prior to global relaminarization, leading to the intermittent occurrence of turbulence in an otherwise laminar flow [1]. For cylindrical pipe flow driven by either a fixed pressure gradient or a fixed mass flux, this intermittency manifests itself as disordered sequences of so-called *puffs*, i.e., turbulent structures filling the cross-section of the pipe but localized in the streamwise direction [2]. The self-organization of these trains of puffs near criticality results from the interplay between local relaminarization events and spatial proliferation [3,4]. For planar shear flows such as plane Couette or plane Poiseuille flow, or any combination of both [5], intermittency usually manifests itself as spatially periodic patterns of laminar-turbulent coexistence in the form of *stripes* of turbulence [6,7]. These stripes display a nonzero angle with respect to the streamwise direction. Closer to the onset of turbulence, these oblique structures have been reported to break up into disjoint finite-sized turbulent spots whose interaction raises interesting questions from a phase transition point of view [8,9]. Despite recent progress coming mainly from low-order models [1,10], a general explanation for these different types of self-organization is still lacking.

Identifying the conditions that lead either to puff-like or stripe-like structures in a given flow geometry would help to unravel the mechanisms responsible for the localization of turbulence. This ambitious task suggests that a flow case should be selected with a free parameter able to bridge as continuously as possible the two limiting cases of turbulent puffs, on one hand, and turbulent stripes on the other hand. In the context of pressure-driven flows, annular Poiseuille flow (aPf) is an interesting candidate for such a homotopy procedure. This geometry features two long (ideally infinite) coaxial pipes of different radii R_i and R_o ($> R_i$) (see Fig. 1), between which an incompressible flow is maintained using a fixed axial pressure gradient. This flow geometry is relevant in many important industrial processes ranging from nuclear plants to heat exchangers. As in all pressure-driven flows, the dramatic drop in flow rate associated with the laminar-turbulent transition makes the issues of whether and how turbulence maintains itself important for practical situations. The shape of the associated laminar flow profile depends only on the radius ratio $\eta = R_i/R_o$. This

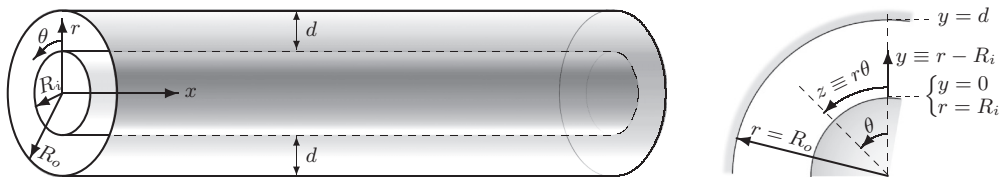


FIG. 1. Configuration of annular Poiseuille flow and coordinate system.

profile turns out to be linearly stable even for values of the Reynolds number far above those where turbulence starts to be sustained, making the transition in this flow case clearly subcritical for all values of η [11,12]. In a former paper [13], the zoology of the different manifestations of laminar-turbulent coexistence was addressed using numerical simulation in moderately long (axially periodic) domains: while helical stripe patterns dominate the low-Re range for $\eta \geq 0.5$, only statistically axisymmetric turbulent structures were identified for $\eta = 0.1$ and low enough Reynolds number. The former type corresponds to the stripes found in plane Poiseuille flow (pPf) in the presence of a wall curvature that vanishes asymptotically as $\eta \rightarrow 1^-$. The latter type can be assimilated to puffs as in circular pipe flow, except that the presence of the inner rod implies a different velocity profile both in the laminar and turbulent zones. Simulations for intermediate $\eta = 0.3$ featured new axially localized helical structures baptized “helical puffs.”

In the present numerical study, we consider all these intermittent regimes in numerical domains longer than in previous studies, parametrized as before by the radius ratio η with emphasis on the patterning property of localized turbulence. Another important control parameter is the Reynolds number $\text{Re}_\tau = u_\tau d / (2\nu)$, where $u_\tau = \sqrt{\tau / \rho}$ is the friction velocity, with τ the mean total wall friction proportional to the pressure gradient and ρ is the density of fluid, ν its kinematic viscosity, and $d = R_o - R_i > 0$ measures the spacing between the two cylinders. The details of the numerics are given in Sec. II. The dynamics of the flow at marginally low values of Re_τ is analyzed in Sec. III for various values of η from 0.1 to 0.5. In Sec. IV, a statistical analysis of the transition from puffs to stripes as η increases is suggested, based on the statistical quantification of the large-scale flows present at the laminar-turbulent interfaces. Eventually, the generality of the transition mechanism advanced in Sec. IV is discussed in Sec. V.

II. NUMERICAL SIMULATION

The geometry is best described using the classical cylindrical coordinate system (r, θ, x) , where the x axis is the axis common to both cylinders. We also define the rescaled azimuthal coordinate $z = r\theta$ and the wall-normal distance from the inner wall $y = r - R_i$. At $r = R_o$ we have $y = d$ and an azimuthal extent $L_{zo} = 2\pi R_o$, while for $r = R_i$ we have $y = 0$ and $L_{zi} = 2\pi R_i$ (see Fig. 1). The specific values of L_{zo} and L_{zi} are listed in Table I. Periodicity is considered in both x and θ , with respective spatial periods L_x and 2π , while no slip ($\mathbf{u} = 0$) is imposed at each wall. The flow between the two cylinders is governed by the incompressible Navier-Stokes equations:

$$\nabla \cdot \mathbf{u} = 0, \quad (1)$$

$$\partial_t \mathbf{u} + (\mathbf{u} \cdot \nabla) \mathbf{u} = -\rho^{-1} \nabla p + \nu \nabla^2 \mathbf{u}. \quad (2)$$

Denoting, respectively, by τ_i and τ_o the wall shear rate at the inner and outer wall, the axial pressure gradient at equilibrium reads $d\bar{p}/dx = -(2/d)(\tau_o + \eta\tau_i)/(1 + \eta)$, from which $u_\tau = \sqrt{-\rho^{-1}d\bar{p}/dx}$ and, hence, Re_τ are defined. The numerical algorithm used to solve Eqs. (1) and (2) combines fourth-order finite differences in both x and θ , together with a second-order scheme in r on a nonuniform radial grid. Time stepping is performed using an Adams-Bashforth scheme for the nonlinear terms and a Crank-Nicolson scheme for the wall-normal viscous terms, which results in

TABLE I. Computational conditions for DNS: L_x and L_z are the streamwise and azimuthal lengths ($L_{zi} = 2\pi R_i$ and $L_{zo} = 2\pi R_o$); N_x and N_z the corresponding grid numbers ($z = r\theta$), while N_y is fixed at 128 for all the cases ($y = r - R_i$). Basically, longer L_x with larger N_x were used for DNS at lower Re_τ .

η	0.1	0.2	0.3	0.4	0.5	0.8
Re_τ	46–150	50–150	50–150	52–80	52–150	52–150
L_x/d	51.2–180.0	102.4–166.0	51.2–160.0	102.4–160.0	51.2–80.0	51.2–80.0
$L_{zi}(\eta)/d$	0.70	1.57	2.69	4.19	6.28	25.1
$L_{zo}(\eta)/d$	6.98	7.85	8.98	10.5	12.6	31.4
N_x	2048 or 4096	4096	2048 or 4096	4096	2048	2048
N_z	256	256	512	512	512	1024

a second-order algorithm. Further information about the numerical method employed here can be found in Refs. [13, 14].

All numerical parameters are reported in Table I. The local numerical resolution has been checked in our previous article [13]. The length of the computational domain has been varied between $51d$ and $180d$ depending on the outcome of the simulations. It is longer than most simulations from Ref. [13] in order to capture the interaction between several distinct localized turbulent structures.

III. TEMPORAL DYNAMICS OF LOCALIZED TURBULENT STRUCTURES

The procedure (quenching from the turbulent regime) chosen here is similar to that in Refs. [13, 15]: for each value of η , a statistically steady turbulent flow is first reached easily by adding a random perturbation of finite amplitude to the laminar base flow at $Re_\tau = 150$. For this value of Re_τ , turbulence unambiguously occupies the whole numerical domain. Then, Re_τ is decreased in finite steps until statistically steady laminar-turbulent coexistence is detected from visualizations, usually around $Re_\tau \approx 80$. The control parameter is then lowered further in smaller steps until turbulence globally collapses, typically for $Re_\tau \lesssim 50$. Let us denote by $Re_\tau^c = Re_\tau^c(\eta)$ the critical value of Re_τ below which no turbulence is sustained in the long time limit. Throughout this paper, the superscript $(\cdot)^c$ will be used to represent a critical point for the sustainment of localized turbulence. However, the values suggested in this paper are not based on a full but costly statistical analysis—like, e.g., in Ref. [3]—but are estimated from our limited set of simulations. We describe below the different types of spatiotemporal dynamics encountered around Re_τ^c in order of increasing η . Note again that all simulations have been performed here in longer domains than in Ref. [13] and that the spatiotemporal regimes resulting from the interaction between different localized patches of turbulence are more complex than in previous works. All the spatiotemporal diagrams shown in this section involve the streamwise velocity averaged azimuthally $\langle u_x/u_\tau \rangle_\theta = \int_0^{2\pi} u_x d\theta / 2\pi$, evaluated at midgap.

A. Localized puffs for $\eta = 0.1$

We describe first the regimes found for low $\eta = 0.1$. Laminar-turbulent coexistence is easily visualized using spatiotemporal diagrams of the quantity $\langle u_x/u_\tau \rangle_\theta$ at midgap as a function of the streamwise coordinate x and of the time t in units of d/u_τ . For easier visualization, the reduced streamwise coordinate x' is used instead of x , where $x' = (x - ct)/d$ with c an adjustable streamwise speed. This speed of the reference frame was adjusted simply by eye in order to cancel out the apparent drift of puffs. It should be noted that the present c does not rigorously correspond to the propagation speed of puffs. Figures 2(a)–2(e) show such diagrams for $Re_\tau = 56, 52, 50, 48,$ and 46 , respectively, with the color map adjusted so that the red color is an indicator of local turbulent motion. For $Re_\tau = 56$, the flow consists of a train of four or five several puffs interacting via sequences of replication and merging events. At $Re_\tau = 52$ and 50 , the number of puffs interacting drops to two

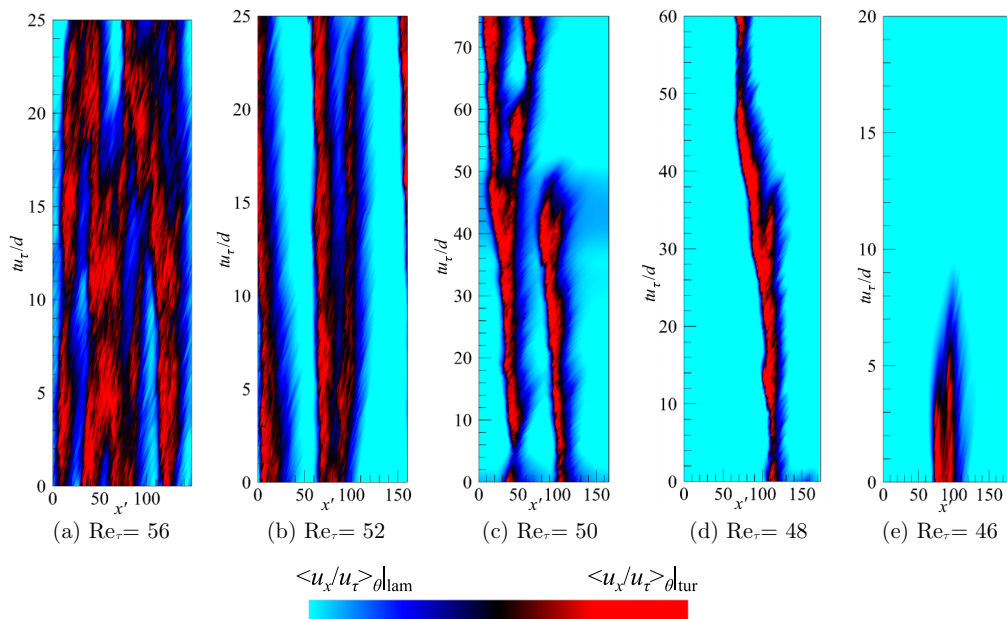


FIG. 2. Space-time diagram of azimuthally averaged streamwise velocity at midgap for $\eta = 0.1$ and different Re_τ . Color map of $\langle u_x/u_\tau \rangle_\theta$ is plotted against a reduced variable $x' = (x - ct)/d$, in a moving frame of reference, and its range is $(\langle u_x/u_\tau \rangle_\theta|_{\text{tur}}, \langle u_x/u_\tau \rangle_\theta|_{\text{lam}})$: (a) (18, 22), (b) (19, 24), (c) (20, 25), (d) (21, 25), and (e) (21, 25).

or three, with relaminarization or replication (“splitting”) events occurring on longer timescales and no merging event. For $\text{Re}_\tau = 48$, a single isolated puff survives over the whole observation time, though at several occasions its internal fluctuations bring it close to splitting or to collapsing. For $\text{Re}_\tau = 46$, the isolated puff attempts to split into two parts that both collapse after less than $5d/u_\tau$. This description is completely consistent with that of turbulent puffs in circular pipe flow in Refs. [3,16,17]. This suggests, though it remains to be properly shown, that the transition in an infinitely long pipe would be continuous, with the critical point Re_τ^c for this value of η lying around 48 ± 1 .

Detailed visualization of the flow structures is achieved using the spatial fluctuations of the radial velocity u'_r around its spatial average in a cylinder at arbitrary y . The fluctuating component is defined as

$$u'_i = u_i - \tilde{u}_i(r, t), \quad (3)$$

$$\tilde{u}_i(r, t) = \frac{1}{L_x 2\pi} \iint u_i(x, r, \theta, t) dx d\theta. \quad (4)$$

Note that \tilde{u}_i does not necessarily equal the laminar flow because of the presence of fully/localized turbulent region in our case—in particular, an oblique turbulent region is also accompanied by a large-scale flow also in the azimuthal direction, which may provide nonzero \tilde{u}_θ [13]. The flow structures for $\text{Re}_\tau = 56$ and 52 are visualized in Fig. 3. These figures confirm the resemblance with puffs from circular pipe flow (see, e.g., Ref. [17] for similar visualizations of puffs close to the onset of puff splitting). In particular, each patch of turbulent fluctuations extends over the full cross-section, i.e., they are rather homogeneous in the z direction with straight laminar-turbulent interfaces.

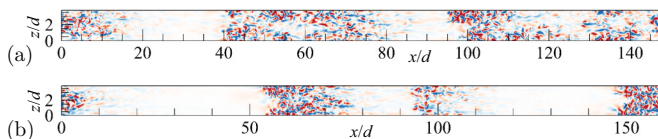


FIG. 3. Two-dimensional contours of instantaneous u'_r (blue, red) = $(-0.75, 0.75)$ at midgap, for $\eta = 0.1$ at $\text{Re}_\tau =$ (a) 56 and (b) 52. The mean flow direction is from left to right.

B. Occurrence of helical puffs for $\eta = 0.2$ and 0.3

Visualizations of the intermittent flow structures and their temporal dynamics for $\eta = 0.2$ are shown in Figs. 4 and 5 using the same quantities as in Figs. 2 and 3. The spatiotemporal diagrams for $\text{Re}_\tau = 56, 52,$ and 50 in Figs. 4(a)–4(c) do not differ much from those for $\eta = 0.1$, except perhaps at $\text{Re}_\tau = 56$, where the turbulent flow exhibits a stronger tendency toward patterning (emergence of a well-defined streamwise wavelength) than for lower η . For $\eta = 0.2$, the puff sustaining at $\text{Re}_\tau = 52$ may split and avoid collapse, while the puff at $\text{Re}_\tau = 50$ decays completely; see Figs. 4(b) and 4(c). This suggests a critical point around $\text{Re}_\tau^c = 51 \pm 1$. The spatial fluctuations of $u'_r(x, z)$ at midgap in Fig. 5 show a surprising property: some of the laminar-turbulent interfaces identified display obliqueness with respect to the streamwise direction while other do not.

Similar data for $\eta = 0.3$ confirms the above-mentioned trends, with an even stronger patterning property and a comparable critical value: Fig. 6(c) provides specific evidence that, for $\text{Re}_\tau = 50$, three puffs separated by a comparable wavelength collapse in synchrony. The occurrence of oblique laminar-turbulent interfaces appears also more pronounced, judging from the fluctuations of u'_r shown in Fig. 7. The resulting intermittent regime for $\eta = 0.2$ and 0.3 appears hence as a mixture of both classical straight puffs analogous to those found for $\eta = 0.1$ and helical puffs as identified in Ref. [13] in shorter domains. We emphasize the coexistence in space as in time and for a given set of parameters, of both types of structures. This immediately suggests that the transition from (straight) puffs to (oblique/helical) stripes cannot be treated as deterministic but rather requires a statistical treatment. The statistical analysis to be presented in Sec. IV C will be based on the probability density function of large-scale azimuthal velocities that is related to the obliqueness of the pattern.

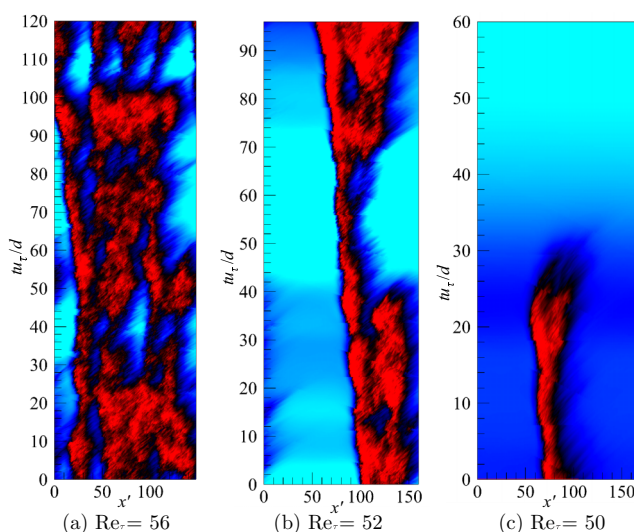


FIG. 4. Same as Fig. 2, but for $\eta = 0.2$: $(\langle u_x/u_\tau \rangle_\theta|_{\text{tur}}, \langle u_x/u_\tau \rangle_\theta|_{\text{lam}})$ = (a) (18, 23), (b) (20, 25), and (c) (20, 27).

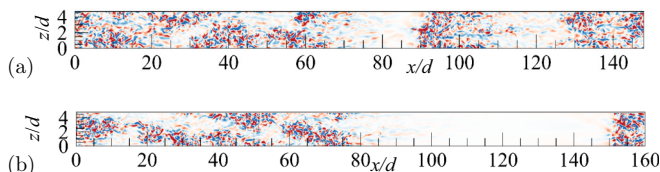


FIG. 5. Same as Fig. 3, but for $\eta = 0.2$ at $Re_\tau =$ (a) 56 and (b) 52.

C. Occurrence of stripe patterns for $\eta \geq 0.4$

Finally, the same indicators have been computed for $\eta = 0.4$ and 0.5 at $Re_\tau = 56$ and 52 , both apparently above the corresponding value of Re_τ^c . The associated spatiotemporal diagrams demonstrate sustained patterning and are not shown. The spatial fluctuations shown for randomly chosen snapshots in Figs. 8 and 9 show exclusively oblique laminar-turbulent interfaces for $Re_\tau = 56$ and apparently no puff-like structures, suggesting that this corresponds to the periodic stripe regime. In contrast, $Re_\tau = 52$ shows a sequence of isolated spots less like a periodic pattern. A similar dynamics was reported in planar cases ($\eta \rightarrow 1$) where for marginally low values of Re_τ the stripe patterns break up into smaller structures [18], and this is a feature specific to the turbulent regimes slightly above Re_τ^c .

IV. BIFURCATION ANALYSIS BASED ON LARGE-SCALE FLOWS

Bifurcations from one turbulent regime to another one are difficult to investigate because, unlike bifurcations of exact steady/periodic states, the presence of turbulent fluctuations both in time and space makes the choice of a well-defined bifurcation parameter nonobvious. We intend here to characterize the bifurcation of the *shape* of coherent structures, where no particularly obvious Eulerian indicator emerges to describe for instance the obliqueness of the interfaces. We suggest to link the present study to the limiting planar case $\eta \rightarrow 1$, which has been already discussed in Ref. [19], and to generalize it to curved geometries corresponding to $0 < \eta < 1$. This represents an opportunity to test the limitations of the planar theory in the presence of finite curvature. In

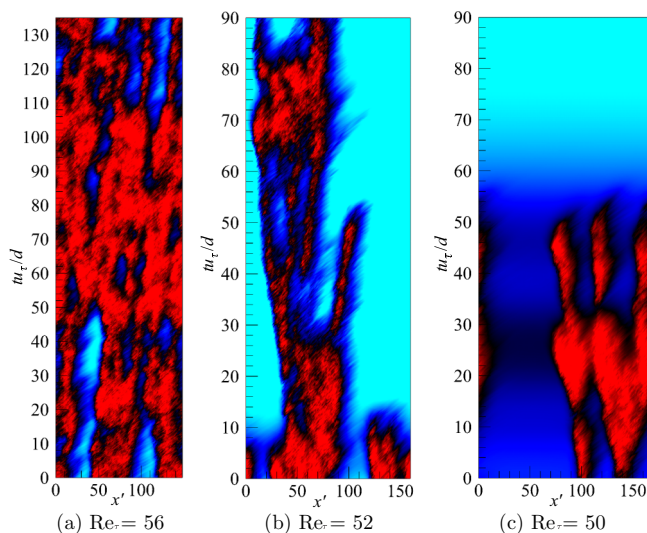


FIG. 6. Same as Fig. 2, but for $\eta = 0.3$: $(\langle u_x/u_\tau \rangle_\theta|_{\text{tur}}, \langle u_x/u_\tau \rangle_\theta|_{\text{lam}}) =$ (a) (18, 22), (b) (19, 23), and (c) (19, 26).

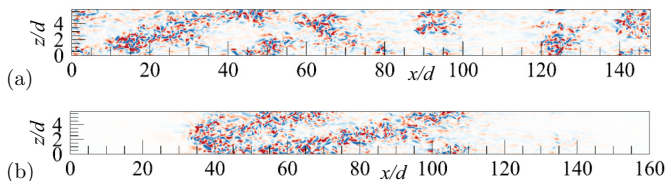


FIG. 7. Same as Fig. 3, but for $\eta = 0.3$ at $\text{Re}_\tau =$ (a) 56 and (b) 52.

addition, we keep in mind the observation that both types of structures, straight and helical, have been detected for the same parameters at intermediate values of η . The relevant bifurcation parameter chosen should hence be quantified in a probabilistic manner, with statistics carried out, for each set of parameters η and Re_τ , over both time and space.

A. Role of the large-scale flows

For planar flows, it was suggested in Ref. [19] that the obliqueness of interfaces could be explained qualitatively by the existence of *large-scale flows*. In the presence of a sufficiently marked scale separation between small scales (the turbulent fluctuations) and large scales, it was shown analytically that large scales advect the small scales of weakest amplitude. Interfaces between laminar and turbulent motion correspond precisely to the zones where the fluctuations decay from their turbulent amplitude toward zero. It is thus expected that the planar orientation of the interface corresponds precisely to the orientation of the large-scale flow advecting the small scales at the edges of the turbulent patches. In particular, the global angle of the periodic stripe patterns corresponds accurately to the angle of the large-scale flow (cf Fig. 2(c) in Ref. [19]): a nonzero angle is linked to the existence of a *spanwise* component for the large scales. The small scales of interest consist essentially of streaks and streamwise vortices of finite length, which form the minimal ingredients of the self-sustaining process in all wall-bounded shear flows [20]. The origin of the transverse large scale flow is kinematic rather than dynamic: it can be derived from the mass conservation at the interfaces once streamwise localization is assumed. In particular, the role of the spanwise large-scale component in the planar case is to compensate for the loss of streamwise flow rate inside the turbulent patch (with respect to the reference flow rate inside the laminar zones).

We begin by defining the relevant quantities with notations adapted to the present cylindrical geometries for any value of η . Independently of temporal considerations, large-scale flows $\mathbf{U}(x, r, \theta)$ can be obtained from any flow field $\mathbf{u}(x, r, \theta)$ by the application of a low-pass filter \mathcal{L} that selects only the lowest-order modes in θ and x directions. The spectral cutoff criterion in these two directions is an intrinsic parameter of the filter. The exact choice of the kernel for the low-pass filter (here Heaviside functions in both wave numbers k_x and k_θ) matters little as long as the scale separation is sufficiently well pronounced. Consider the continuity equation in cylindrical coordinates:

$$\partial_x u_x + \frac{1}{r} \partial_r (r u_r) + \frac{1}{r} \partial_\theta u_\theta = 0. \quad (5)$$

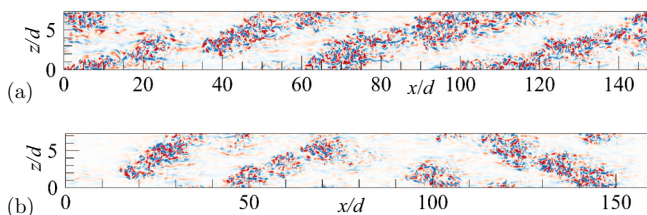
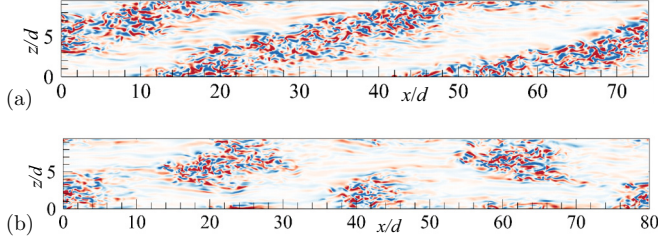


FIG. 8. Same as Fig. 3, but for $\eta = 0.4$ at $\text{Re}_\tau =$ (a) 56 and (b) 52.


 FIG. 9. Same as Fig. 3, but for $\eta = 0.5$ at $\text{Re}_\tau =$ (a) 56 and (b) 52.

The divergence operator commutes with \mathcal{L} , which leads to the same equation for the large-scale flow:

$$\partial_x U_x + \frac{1}{r} \partial_r (r U_r) + \frac{1}{r} \partial_\theta U_\theta = 0. \quad (6)$$

Multiplying Eq. (6) by r and integrating it from $r = R_i$ to R_o leads to

$$\int_{R_i}^{R_o} \partial_\theta U_\theta dr = - \int_{R_i}^{R_o} \partial_x U_x r dr. \quad (7)$$

We now define radial integration

$$\overline{(\cdot)} = \frac{\int_{R_i}^{R_o} r(\cdot) dr}{\int_{R_i}^{R_o} r dr}. \quad (8)$$

Since $\overline{U_x}$ does not vanish, then we can define an angle $\alpha \geq 0$ with respect to the streamwise direction by

$$\tan \alpha(x, \theta, t) = \left| \frac{\overline{U_\theta(x, \theta, t)}}{\overline{U_x(x, \theta, t)}} \right|. \quad (9)$$

B. Spectral analysis

In order to evaluate which large-scale components are present here, time-averaged pre-multiplied energy spectra evaluated at midgap are shown in Fig. 10 for $\text{Re}_\tau = 56$ (for which all flows are spatially intermittent) and for different values of η from 0.1 to 0.8. Energy spectra are based on the two-dimensional Fourier transform $\widehat{u}_i(k_x, y, k_z)$ of $u'_i(x, y, z)$ with respect to x and z , for all y . The *streamwise* one-dimensional spectra associated with the streamwise and azimuthal velocity fluctuations u'_x and u'_θ are defined, respectively, by

$$E_{xx}(k_x, y) = \frac{L_x L_z}{(2\pi)^2 T} \int_t^{t+T} \int_0^\infty \Re(\widehat{u}_x \widehat{u}_x^*) dk_z dt, \quad E_{\theta\theta}(k_x, y) = \frac{L_x L_z}{(2\pi)^2 T} \int_t^{t+T} \int_0^\infty \Re(\widehat{u}_\theta \widehat{u}_\theta^*) dk_z dt. \quad (10)$$

The asterisk represents complex conjugation, T is the averaging time, and \Re denotes the real part. The proportionality constant is chosen so that

$$\int E_{xx}(k_x) dk_x = \int E_{xx}(k_z) dk_z = \langle u'_x u'_x \rangle, \quad \int E_{\theta\theta}(k_x) dk_x = \int E_{\theta\theta}(k_z) dk_z = \langle u'_\theta u'_\theta \rangle, \quad (11)$$

as function of either k_x or k_θ , where averaging $\langle \cdot \rangle$ is performed over x , θ , and t .

Careful analysis of Fig. 10 reveals robust features. Small scales associated with turbulent fluctuations are present around $\lambda_x/d \approx 2-3$ and $\lambda_z/d \approx 1$ in all directions for all components. The situation is different for large-scale velocity components: out of the four figures in Fig. 10, only

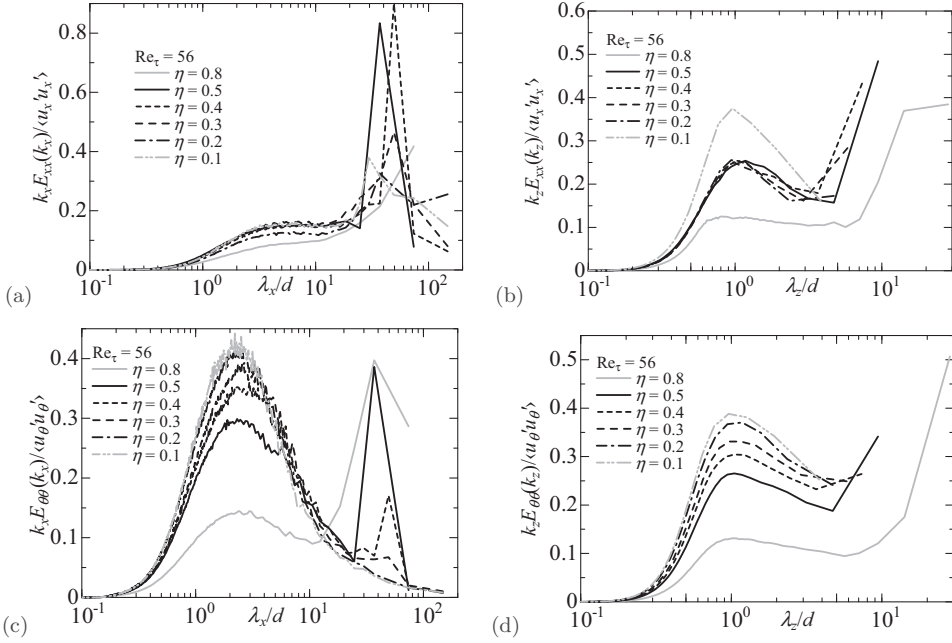


FIG. 10. Premultiplied energy spectra for u'_x and u'_θ as a function of either wavelength λ_x/d or λ_z/d at mid-gap: (a) streamwise spectra of u'_x , (b) spanwise spectra of u'_x , (c) streamwise spectra of u'_θ , and (d) spanwise spectra of u'_θ . The streamwise and azimuthal wave numbers are defined as $k_x = 2\pi/\lambda_x$ and $k_z = 2\pi/\lambda_z$, respectively. The spectra are normalized by an ensemble-averaged value of $u'_i u'_i$ at midgap.

u_x as a function of x displays large scales for all value of η . These large scales do not appear strongly separated from the smaller ones and are located at $\lambda_x/d \approx 15-70$. Neither u_θ as a function of either x or θ , nor u_x as a function of θ , possesses such a robust large-scale component. Only as η exceeds 0.3 do well-separated peaks at similar large scales emerge in each spectrum. Important information can be deduced from these spectra. First, should large scales be found, the corresponding cutoff can be located safely in the intervals $\lambda_x^c/d \approx 10-20$ and $\lambda_z^c/d \approx 2-5$. Second, by construction the wavelengths in the spectra are limited by the box dimensions L_x and L_z . A clear difference emerges between Figs. 10(a) and 10(c) on one hand (showing the λ_x dependence) and Figs. 10(b) and 10(d) on the other hand (showing the λ_z dependence): in the latter case the occurrence of an azimuthal large-scale peak for both x and θ components is ruled out when $L_z \ll \lambda_z^c$. In other words, the spanwise large-scale component is present only for sufficient azimuthal extent, whereas streamwise large-scale modulations are always present as long as the flow features spatial intermittency. We emphasize here that the azimuthal extent should be measured in units of $d = R_o - R_i$, since streaks and streamwise vortices (forming the small scales) scale with the gap size d rather than with any of the two radii R_o or R_i . Wall units are another candidate, but large-scale structures of interest are generally considered to scale with outer units. Our hypothesis here is that the occurrence of azimuthal large-scale flows depends directly on the azimuthal extent L_z/d , itself a function of η .

The quantity L_z , however, depends on the value of r . It is simpler to focus on the inner and outer azimuthal extents L_{zi} and L_{zo} , given, respectively, by

$$L_{zi} = 2\pi d \frac{\eta}{1-\eta}, \quad (12)$$

$$L_{zo} = 2\pi d \frac{1}{1-\eta}. \quad (13)$$

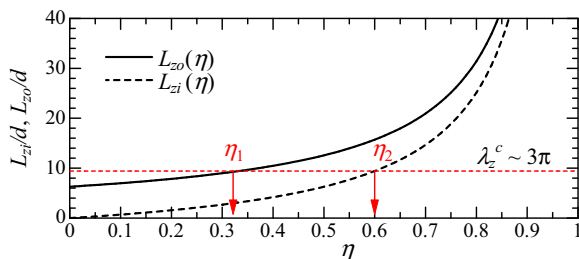


FIG. 11. Azimuthal length as a function of radius ratio.

Both quantities (expressed in units of d) are plotted as functions of the radius ratio η in Fig. 11.

Let us fix rather arbitrarily a cutoff value λ_z^c . The intersection of the horizontal line $L_z = \lambda_z^c$ with the curves $L_{zo}(\eta)$ and $L_{zi}(\eta)$ in Fig. 11 defines two values of η , respectively, η_1 and η_2 . This leads to three distinct ranges of values for η :

(1) for $0 < \eta \leq \eta_1$, there is no space for large scales in the azimuthal direction, neither at the inner nor at the outer wall. As a consequence, $\overline{U_\theta} = 0$ for all r , and $\partial_x \overline{U_x} = 0$.

(2) for $\eta_2 \leq \eta \leq 1$, azimuthal large scales can form at both inner and outer walls: $\partial_\theta \overline{U_\theta} = -\partial_x \overline{U_x}$ with $\overline{U_\theta} \neq 0$. The situation is then analogous to the planar case.

(3) for $\eta_1 \leq \eta \leq \eta_2$, the situation is mixed: azimuthal large scale flows cannot be accommodated at all locations in the cross-section. A probabilistic approach is required.

For instance, choosing $\lambda_z^c/d = 3\pi$ leads to $\eta_1 = 1/3$ and $\eta_2 = 3/5$, which is consistent with our observations. While the classification above is not useful in practice to predict accurately the transition thresholds η_1 and η_2 [mainly because of the difficulty to define a unique cutoff value $\lambda_z^c(\text{Re}_\tau)$], it captures the main physical idea: the presence of confinement in the azimuthal direction defines the two extreme regimes of straight interfaces (associated with puffs) or oblique interfaces (associated with oblique stripes). In addition, there is a range of value of η for which there is a probability of observing both types of interfaces (and hence both puffs and stripes) in the same flow at different times and/or different positions.

It can be useful to investigate cross-sections of the flow in the different regime to understand the implications of the previous hypothesis. The two-dimensional contours of u'_x and u'_θ in arbitrary chosen $(r-\theta)$ cross-sections are shown in Figs. 12 and 13, respectively, for different values of η .

The isocontours of u'_x in Fig. 12 allow one to count the numbers of streaks present in the vicinity of each wall. Each of these streaks has a radial and azimuthal extent $\approx d/2$, and the analysis of the spectra in Fig. 10 also suggests that their streamwise extent is approximately $2d$. In principle, one would expect the streak size to scale in inner units v/u_τ ; however, the range of values of Re_τ investigated here is relatively narrow and we prefer to report the dimensions of the streaks in (outer) units of d , as the relation $\lambda_z \approx d$ emphasizes their quasicircular cross-section. In the case of the straight puffs found for $\eta = 0.1$, u'_x shows no large-scale azimuthal modulation, while high-order modulations (streaks) can be easily noted. With increasing η , the number of streaks increases as the azimuthal extent increases, a supplementary confirmation that the relevant lengthscale here is d rather than R_o or R_i . For $\eta = 0.5$ and 0.8 [Figs. 12(d) and 12(e)], the low-order nonaxisymmetric modulation of u'_x is the direct signature of the helix-shaped turbulence. To a lesser degree, such a modulation can also be visually detected for $\eta = 0.2$ and 0.3 [Figs. 12(b) and 12(c)]. Similar conclusions can be drawn from the isocontours of u'_θ in Fig. 13 as well.

C. Statistics of transverse large-scale flows

This section is now devoted to a quantitative investigation of the orientation of the large-scale flow near the interfaces for varying radius ratio η . We begin by describing in more detail how data from

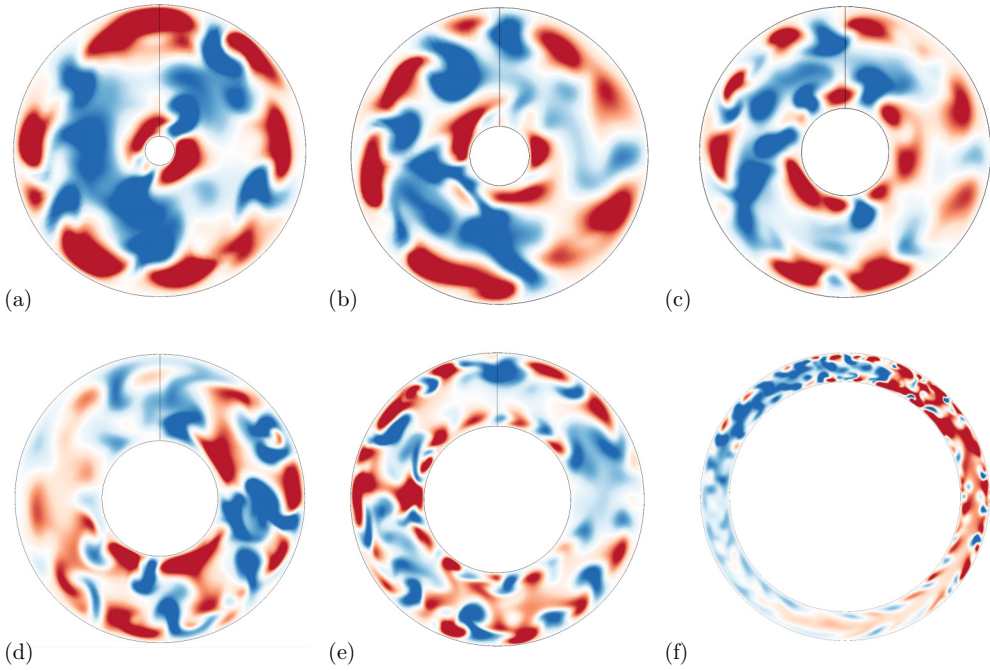


FIG. 12. Two-dimensional cross-sections (r, θ) of instantaneous u'_x for $\eta =$ (a) 0.1, (b) 0.2, (c) 0.3, (d) 0.4, (e) 0.5, and (f) 0.8 at $\text{Re}_\tau = 52$. Color map from $-3u_\tau$ (blue) to $+3u_\tau$ (red).

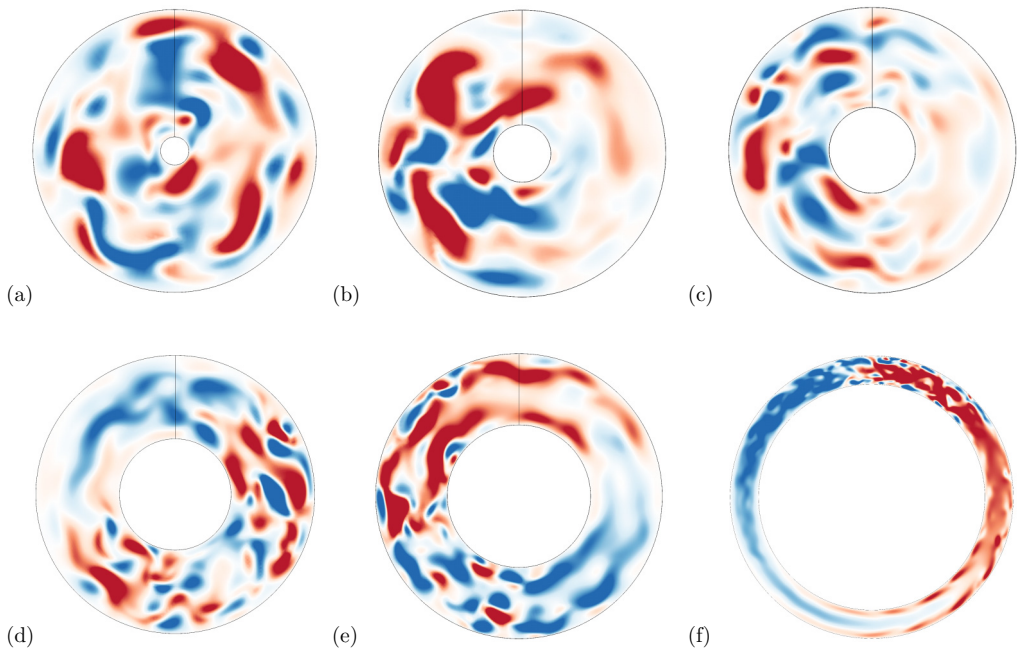


FIG. 13. Two-dimensional cross-sections (r, θ) of instantaneous ru'_θ for $\eta =$ (a) 0.1, (b) 0.2, (c) 0.3, (d) 0.4, (e) 0.5, and (f) 0.8 at $\text{Re}_\tau = 52$. Color map from $-1u_\tau$ (blue) to $+1u_\tau$ (red): the positive direction of θ is clockwise in the plots.

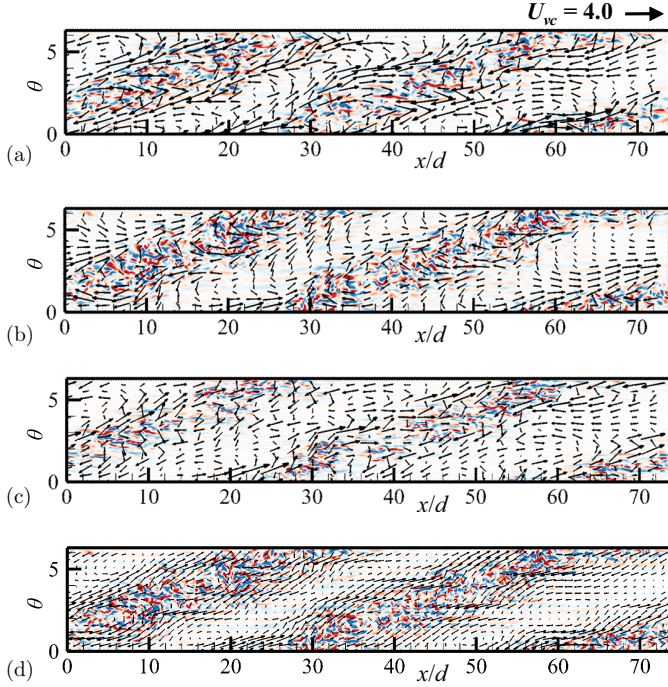


FIG. 14. Two-dimensional contours of instantaneous u'_r (blue, red) $= (-1.0, 1.0)$ and large-scale flow (U_x, rU_θ) as vectors at $y/d =$ (a) 0.19, (b) 0.5, and (c) 0.81, for $\eta = 0.5$ and $\text{Re}_\tau = 56$. Wall-normal-averaged large-scale flow $(\overline{U_x}, \overline{U_\theta})$ with contours of u'_r at midgap is shown in (d). The reference-vector length U_{VC} is shown in the top right of (a).

the previous direct numerical simulations is post-processed. Based on the apparent scale separation in the spectra from Fig. 10, we consider a low-pass filter \mathcal{L} whose kernel in spectral (k_x, k_z) space is non-zero only for

$$|k_x| \leq \frac{2\pi}{20d}, \quad |k_z| \leq \frac{2\pi}{2d}. \quad (14)$$

The original velocity fields $\mathbf{u}(x, r, \theta, t)$ are transformed via \mathcal{L} into filtered fields $\mathbf{U}(x, r, \theta, t)$. The two-dimensional wall-integrated large-scale flow $(\overline{U_x}, \overline{U_\theta})$ is then computed using the definitions in Eq. (8).

An instantaneous snapshot of the large-scale flow $\mathbf{U}(x, r, \theta, t)$ is plotted for several values of r together with its wall-integrated counterpart, namely, $\overline{U_x}(x, \theta, t)$ and $\overline{U_\theta}(x, \theta, t)$. The cases $\eta = 0.5$ and $\eta = 0.1$ are, respectively, shown in Figs. 14 and 15. These plots highlight the genuinely three-dimensional structure of the velocity field \mathbf{U} . For $\eta = 0.5$, where turbulence clearly takes a helical shape, it can be verified that the local orientation of \mathbf{U} does not necessarily match that of the laminar-turbulent interface. The two-dimensional counterpart $(\overline{U_x}, \overline{U_\theta})$, however, does point in a direction parallel to the interface, which confirms the previous hypothesis about the role of the large-scale flows. The situation is less clear in the puff case in Fig. 15. Unlike for higher η no robust oblique large-scale flow can be found, neither on arbitrary- r cylinders nor for the wall-integrated field $(\overline{U_x}, \overline{U_\theta})$.

Let us focus also on the local angle α of the large-scale flow defined by Eq. (9), in addition to the azimuthal velocity component $\overline{U_\theta}$ alone. Both quantities are functions of (x, θ) position and time. Statistics of $\overline{U_\theta}$ and α have been gathered for all parameters over the numerical grid (x_i, z_j) and over different times. Since we are mainly interested in the values of $\overline{U_\theta}$ at the laminar-turbulent

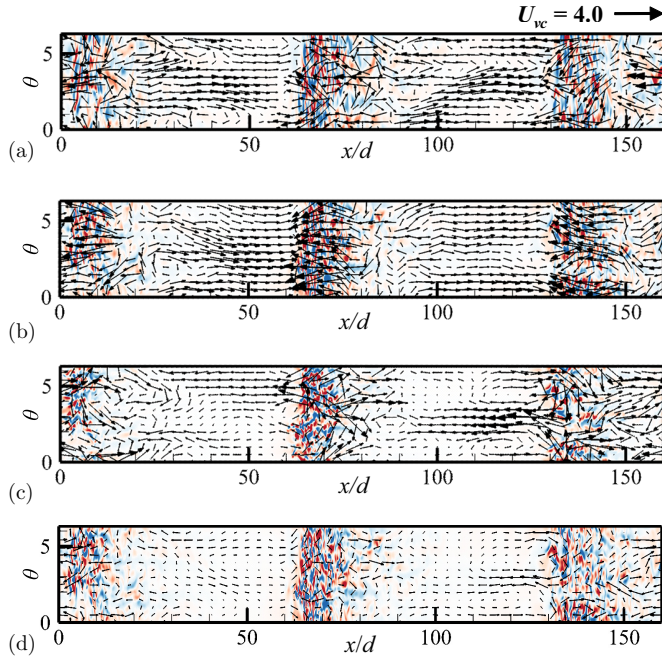


FIG. 15. Same as Fig. 14, but at $y/d =$ (a) 0.25, (b) 0.5, and (c) 0.75, for $\eta = 0.1$ and $\text{Re}_\tau = 56$.

interfaces, we exclude from the statistics fully laminar portions of the flow which would overestimate the statistical weight of the $\overline{U}_\theta \approx 0$ contribution. This is achieved by conditioning all statistics by the additional constraint $|u'_r|/u_\tau > 0.2$ (which is never fulfilled in laminar zones where $u'_r \approx 0$). Probability distribution functions (PDFs) for $|\overline{U}_\theta|$ and α are obtained by considering bins of width $\Delta\overline{U}_\theta = 0.025$ and $\Delta\alpha = 0.25$.

We first describe the PDFs of $|\overline{U}_\theta|$ (normalized by u_τ) obtained for several values of η and parametrized by Re_τ , and shown in Fig. 16(a). For $\eta = 0.1, 0.2$, and 0.3 , the PDF looks reasonably Gaussian. This excludes statistically significant nonzero values of the azimuthal component. Note that we are here only considering the radially integrated azimuthal large-scale velocity component, which in principle does not exclude local weak “zonal” flows [21] with an almost vanishing radial average. For increasing values of $\eta \geq 0.3$, the tendency for the PDF to flatten away from zero becomes stronger, thereby enlarging the range of values of $|\overline{U}_\theta|$. For $\eta = 0.4$, a new peak emerges in the PDF from the former tail in the range $\overline{U}_\theta = 0.2\text{--}0.3u_\tau$, and this peak overweighs clearly the $\overline{U}_\theta = 0$ contribution for $\eta \geq 0.5$. This shows how increasing η beyond 0.3 leads with increasing probability to the emergence of a transverse large-scale flow component, interpreted as responsible for the oblique interfaces observed. Focusing on the lowest values of $\text{Re}_\tau = 52$ and 56 , where intermittency has been observed, we next analyze more quantitatively the PDFs of both $|\overline{U}_\theta|/u_\tau$ and α , parametrized by η in the range 0.1–0.8, cf. Figs. 16(a) and 16(b), with the aim of extracting a comprehensive bifurcation diagram as a function of η .

The transition from a unimodal distribution of both (unsigned) \overline{U}_θ and α cannot be well analysed using standard statistical moments such as the mean and the variance. Instead we can extract, for both distributions, the statistical mode M , i.e., the global maximum of each PDF. They are reported in Figs. 17(a) and 17(b), respectively. In both cases the maximum is at 0 for $\eta \leq 0.3$ and jumps to a nonzero value for the next investigated value, i.e., for $\eta \geq 0.4$. The mode initially increases as η increases, however, we note a decrease of both $M(\overline{U}_\theta/u_\tau)$ and $M(\alpha)$ for the largest value of $\eta = 0.8$. This is due to the flattening of the PDF observed in Fig. 16 due to a wider range of possible angles

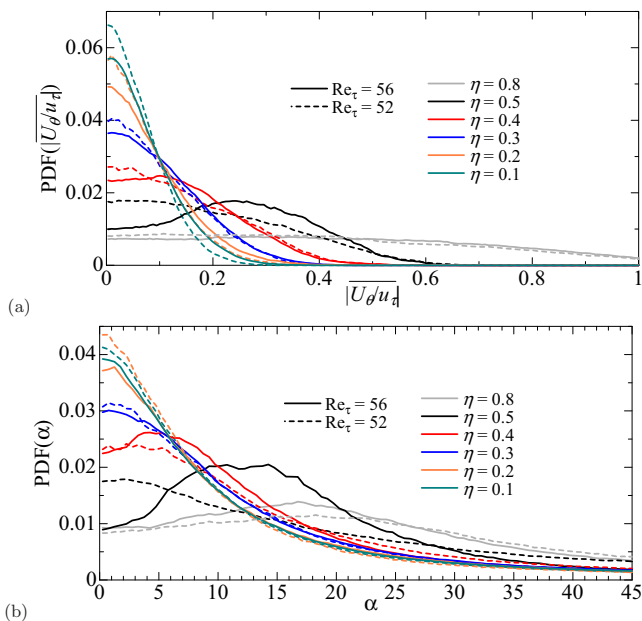


FIG. 16. PDFs of quantities that characterize the azimuthal large-scale flow and laminar-turbulent interface: (a) $|\overline{U_\theta}|/u_\tau$ and (b) α , for $Re_\tau = 52$ and 56 , $\eta = 0.1$ – 0.8 .

(not shown). The statistical mode analysis allows to read directly the typical angles of the oblique stripes of Fig. 17(b). However, it does not yield an accurate value of the critical value $\eta_c(Re_\tau)$ of η at which stripes emerge: all that can be deduced is that η_c lies in the range $[0.3 : 0.4]$. An alternative, specific to the case of unimodal-bimodal transitions, is to measure the convexity of the PDF near the

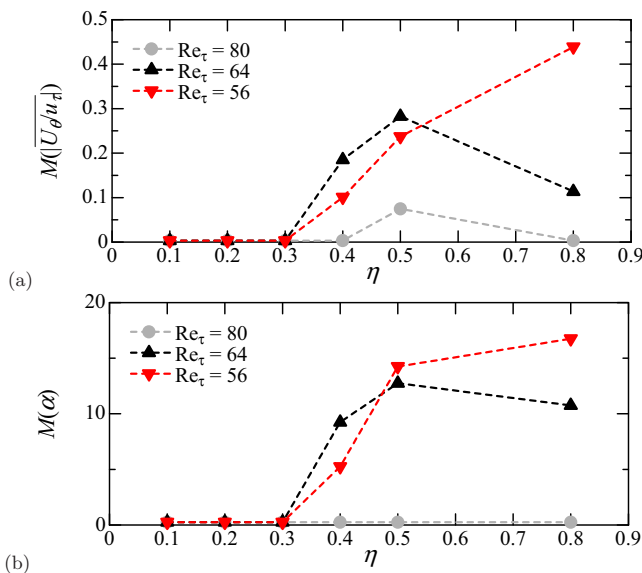


FIG. 17. Statistical mode extracted from the PDFs in Fig. 16 of: (a) $|\overline{U_\theta}|/u_\tau$ and (b) α , for $Re_\tau = 52$ and 56 , $\eta = 0.1$ – 0.8 . The data suggests a critical value of $\eta = \eta_c$ between 0.3 and 0.4 .

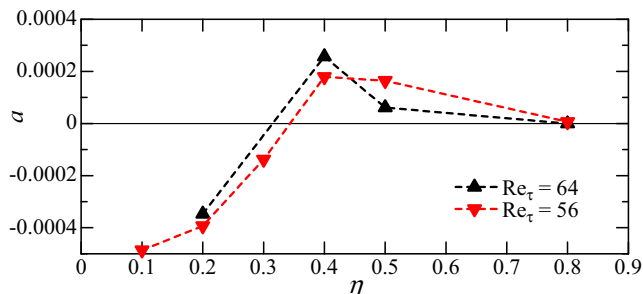


FIG. 18. Coefficient a in Eq. (15) extracted from the PDF of the angle α .

origin. Suppose that the PDFs in Fig. 16 are even functions and can be fitted near the origin $x = 0$ as

$$p(x, \eta, Re_\tau) = ax^2 + c, \quad (15)$$

with $a = a(\eta, Re_\tau)$ and $c = p(0, \eta, Re_\tau)$. The coefficient $a(\eta, Re_\tau)$ is negative for a unimodal distribution centered at $x = 0$ and positive for a bimodal distribution whose maximum lies away from $x = 0$. As a consequence, $a(\eta, Re_\tau) = 0$ can be used to define $\eta_c(Re_\tau)$. The values of $a(\eta, Re_\tau)$ are plotted in Fig. 18 as functions of η parametrized by Re_τ after the PDF of α has been approximated by a quadratic function using a least squares algorithm. Consistently with the mode analysis, η_c lies in the interval $[0.3 : 0.4]$ for both $Re_\tau = 64$ and 56 (the value $Re_\tau = 80$ has been omitted as it is too high to sustain oblique stripes). The present data suggests even a slight decrease of η_c with Re_τ , but this remains to be verified for a larger number of values of Re_τ .

V. DISCUSSION

The present results have confirmed that annular pipe flow (aPf), parametrized by both its radius ratio η and the friction Reynolds number Re_τ , is a relevant candidate to track the transition from puffs to oblique stripes. The main physical mechanism responsible for this transition is the relaxation of the azimuthal confinement (measured in units of the gap d) as η increases, allowing for more freedom in the orientation of the large-scale flow occurring at the laminar-turbulent interfaces, should such interfaces exist. Beyond a critical azimuthal extent, a neater selection of orientations occurs, ruled by the mass conservation at the interfaces. As η increases from 0 to 1, the following turbulent regimes are encountered:

- (1) spatiotemporal intermittency as in circular pipe flow for $0 < \eta \lesssim 0.2$.
- (2) mixed distribution of straight and helical puffs for $0.2 \lesssim \eta \lesssim 0.4$.
- (3) regular patterns of oblique stripes, so-called helical turbulence, for $\eta \gtrsim 0.5$.
- (4) disordered patterns of oblique stripes for $0.5 \ll \eta \lesssim 1$.

The last item has not been verified here but is expected to match all observations in extended planar shear flows (with additional effects due to the small wall curvature). This apparent disorganisation occurs when the transverse extent is sufficiently larger than the correlation length of the intermittent regime, at least sufficiently above the critical point $Re_\tau^c(\eta)$. The parameter space may also contain new regimes so far unexplored. A statistical analysis has been carried out by focusing entirely on the local structure and orientation of the large-scale flow. Note that other approaches are possible to handle bifurcations from one turbulent regime to another one. When the two regimes of interest are characterized by symmetry breaking (as is the case here where each oblique stripe violates the $\overline{U_\theta} = 0$ symmetry), other order parameters can be considered (see, e.g., Ref. [22]). In the spirit of pattern formation, the statistics of some well-chosen spectral coefficient characteristics of the structures under study can be helpful. The transition from full turbulence to stripe patterns or to puffs has been considered precisely in this manner for various shear flows [16,23,24]. Orientation reversals of turbulent stripes in pCf were also monitored by considering the competition between

two or more Fourier coefficients corresponding to different wave vectors [25]. Modal approaches, however, show the strong disadvantage of being domain-dependent. We believe that the current statistical approach, more local than modal, is more adapted to the spatiotemporally intermittent flow regimes encountered here, especially for low η .

While an experimental verification of such flow regimes is called for, it is instructive to discuss whether other shear flow geometries lend themselves easily to bifurcations between intermittently turbulent regimes. The transition from puffs to stripes corresponds essentially, as previously shown, to a transition from one-dimensional to two-dimensional coexistence, via the occurrence of quasi-one-dimensional stripe patterns. Other homotopies can be suggested by similarly tuning the confinement in the direction transverse to the mean flow. Imposing confinement by sidewalls in an otherwise Cartesian geometry is a possible option. A rectangular duct flow driven by a pressure gradient, with a cross-section of dimensions $L_y \times L_z$, can be parametrized both by a Reynolds number and an aspect ratio $A = L_z/L_y$ ($A \geq 1$ by convention). The geometry of $A = 1$ corresponds to a square duct whereas $A \rightarrow \infty$ is equivalent to plane Poiseuille flow. The laminar profile is known to be linearly stable for all values of Re_τ of interest here. This parametric problem has been considered numerically in Ref. [26]. Again straight puffs have been identified for $A \leq 3$, whereas spots with somewhat oblique interfaces have been visualized for $A \geq 4$. The authors have reported a peculiarity of the confinement by solid sidewalls: permanent local relaminarization at the sidewalls affecting the localization of the turbulent structure. This is consistent with the recent experimental observations of spots in a duct flow with aspect ratio $A = 7.5$ [27]. While this system has the advantage of dealing with flat walls only, the local relaminarization at the sidewalls is interpreted as an additional complication obscuring the transition from puffs to oblique stripes.

Other examples closer to the present case of aPf share a common geometry but differ in the way energy is injected into the flow. The Taylor-Couette system, where the two coaxial cylinders rotate with different frequencies Ω_i and Ω_o in the absence of an axial pressure gradient, is such an example. It is known that for $\eta \rightarrow 1$, the case of exact counter-rotation $\mu = \Omega_o/\Omega_i = -1$ corresponds to plane Couette flow, which has a linearly stable base flow. It has been experimentally verified for η slightly below 1 that low-Re regimes with $\mu \approx -1$ feature two-dimensional intermittent arrangements of oblique stripes with both positive and negative angles [6,28,29]. Reducing η with fixed μ , however, leads to changes in the stability of the base flow. Other regimes such as those featuring interpenetrating spirals [30] enter the bifurcation diagram and make the continuation from stripes to puffs unlikely. It is an open question whether other paths in an enlarged parameter space could lead to such a transition.

Finally, an interesting candidate for the continuation from stripes to puffs is the sliding Couette flow (sCf), where the outer cylinder is fixed and the inner one moves axially with a constant velocity (see, e.g., Ref. [31]). This flow is thought to be equivalent to pCf in the $\eta \rightarrow 1$ limit and again to pipe flow in the vanishing η limit. It has been verified numerically [32] that this system bridges puffs to spots in a way apparently similar to the present system. Whether and how the homotopies in sCf and aPf really differ remains an open question. However, aPf shows the important advantage of being easier to achieve experimentally as it does not include any motion of the solid walls, only a pressure gradient imposed on a fixed geometry.

ACKNOWLEDGMENTS

T.I. was supported by a Grant-in-Aid from JSPS (Japan Society for the Promotion of Science), Fellowship No. 26-7477. This work was partially supported by JSPS KAKENHI Grants No. 16H06066 and No. 16H00813. The present simulations were performed on supercomputers at the Cyberscience Centre of Tohoku University and at the Cybermedia Centre of Osaka University. We thank JSPS, CNRS (Centre National de la Recherche Scientifique), and RIMS (Research Institute for Mathematical Sciences) for additional travel support.

- [1] P. Manneville, Transition to turbulence in wall-bounded flows: Where do we stand? *Mech. Eng. Rev.* **3**, 15-00684 (2016).
- [2] I. J. Wygnanski and F. H. Champagne, On transition in a pipe. Part 1. The origin of puffs and slugs and the flow in a turbulent slug, *J. Fluid Mech.* **59**, 281 (1973).
- [3] K. Avila, D. Moxey, A. de Lozar, M. Avila, D. Barkley, and B. Hof, The onset of turbulence in pipe flow, *Science* **333**, 192 (2011).
- [4] D. Barkley, Theoretical perspective on the route to turbulence in a pipe, *J. Fluid Mech.* **803**, P1 (2016).
- [5] L. Klotz, G. Lemoult, I. Frontczak, L. S. Tuckerman, and J. E. Wesfreid, Couette-Poiseuille flow experiment with zero mean advection velocity: Subcritical transition to turbulence, *Phys. Rev. Fluids* **2**, 043904 (2017).
- [6] A. Prigent, G. Grégoire, H. Chaté, O. Dauchot, and W. van Saarloos, Large-Scale Finite-Wavelength Modulation within Turbulent Shear Flows, *Phys. Rev. Lett.* **89**, 014501 (2002).
- [7] T. Tsukahara, Y. Seki, H. Kawamura, and D. Tochio, DNS of turbulent channel flow at very low Reynolds numbers, in *Proceedings of the 4th International Symposium on Turbulence and Shear Flow Phenomena*, edited by J. A. C. *et al.* (Humphrey, Williamsburg, USA, 2005), pp. 935–940, [arXiv:1406.0248](https://arxiv.org/abs/1406.0248).
- [8] Y. Duguet, P. Schlatter, and D. S. Henningson, Formation of turbulent patterns near the onset of transition in plane Couette flow, *J. Fluid Mech.* **650**, 119 (2010).
- [9] G. Lemoult, L. Shi, K. Avila, S. V. Jalikop, M. Avila, and B. Hof, Directed percolation phase transition to sustained turbulence in Couette flow, *Nat. Phys.* **12**, 254 (2016).
- [10] D. Barkley, Simplifying the complexity of pipe flow, *Phys. Rev. E* **84**, 016309 (2011).
- [11] J. E. Walker, G. A. Whan, and R. R. Rothfus, Fluid friction in noncircular ducts, *AIChE J.* **3**, 484 (1957).
- [12] C. J. Heaton, Linear instability of annular Poiseuille flow, *J. Fluid Mech.* **610**, 391 (2008).
- [13] T. Ishida, Y. Duguet, and T. Tsukahara, Transitional structures in annular Poiseuille flow depending on radius ratio, *J. Fluid Mech.* **794**, R2 (2016).
- [14] H. Abe, H. Kawamura, and Y. Matsuo, Direct numerical simulation of a fully developed turbulent channel flow with respect to the Reynolds number dependence, *J. Fluids Eng.* **123**, 382 (2001).
- [15] J. Philip and P. Manneville, From temporal to spatiotemporal dynamics in transitional plane Couette flow, *Phys. Rev. E* **83**, 036308 (2011).
- [16] D. Moxey and D. Barkley, Distinct large-scale turbulent-laminar states in transitional pipe flow, *Proc. Natl. Acad. Sci. USA* **107**, 8091 (2010).
- [17] M. Shimizu, P. Manneville, Y. Duguet, and G. Kawahara, Splitting of a turbulent puff in pipe flow, *Fluid Dyn. Res.* **46**, 061403 (2014).
- [18] X. Xiong, J. Tao, S. Chen, and L. Brandt, Turbulent bands in plane-Poiseuille flow at moderate Reynolds numbers, *Phys. Fluids* **27**, 041702 (2015).
- [19] Y. Duguet and P. Schlatter, Oblique Laminar-Turbulent Interfaces in Plane Shear Flows, *Phys. Rev. Lett.* **110**, 034502 (2013).
- [20] J. M. Hamilton, J. Kim, and F. Waleffe, Regeneration mechanisms of near-wall turbulence structures, *J. Fluid Mech.* **287**, 317 (1995).
- [21] N. Goldenfeld and H.-Y. Shih, Turbulence as a problem in nonequilibrium statistical mechanics, *J. Stat. Phys.* **167**, 575 (2017).
- [22] P.-P. Cortet, A. Chiffaudel, F. Daviaud, and B. Dubrulle, Experimental Evidence of a Phase Transition in a Closed Turbulent Flow, *Phys. Rev. Lett.* **105**, 214501 (2010).
- [23] L. S. Tuckerman, D. Barkley, and O. Dauchot, Statistical analysis of the transition to turbulent-laminar banded patterns in plane Couette flow, *J. Phys.: Conf. Ser.* **137**, 012029 (2008).
- [24] L. S. Tuckerman, T. Kreilos, H. Schrobbsdorff, T. M. Schneider, and J. F. Gibson, Turbulent-laminar patterns in plane Poiseuille flow, *Phys. Fluids* **26**, 114103 (2014).
- [25] J. Rolland and P. Manneville, Pattern fluctuations in transitional plane Couette flow, *J. Stat. Phys.* **142**, 577 (2011).
- [26] K. Takeishi, G. Kawahara, H. Wakabayashi, M. Uhlmann, and A. Pinelli, Localized turbulence structures in transitional rectangular-duct flow, *J. Fluid Mech.* **782**, 368 (2015).
- [27] G. Lemoult, K. Gumowski, J.-L. Aider, and J. E. Wesfreid, Turbulent spots in channel flow: An experimental study, *Eur. Phys. J. E* **37**, 1 (2014).

- [28] D. Borrero-Echeverry, M. F. Schatz, and R. Tagg, Transient turbulence in Taylor-Couette flow, *Phys. Rev. E* **81**, 025301 (2010).
- [29] K. Avila and B. Hof, High-precision Taylor-Couette experiment to study subcritical transitions and the role of boundary conditions and size effects, *Rev. Sci. Instrum.* **84**, 065106 (2013).
- [30] C. D. Andereck, S. S. Liu, and H. L. Swinney, Flow regimes in a circular Couette system with independently rotating cylinders, *J. Fluid Mech.* **164**, 155 (1986).
- [31] K. Deguchi and M. Nagata, Bifurcations and instabilities in sliding Couette flow, *J. Fluid Mech.* **678**, 156 (2011).
- [32] K. Kunii, T. Ishida, and T. Tsukahara, Helical turbulence and puff in transitional sliding Couette flow, in *Proceedings of ICTAM 2016, Montréal, Canada* (IUTAM, 2016).